







Article

Synthesis of a Very High Specific Surface Area Active Carbon and Its Electrical Double-Layer Capacitor Properties in Organic Electrolytes

Zheng Yue ¹, Hamza Dunya ¹, Maziar Ashuri ², Kamil Kucuk ³, Shankar Aryal ³, Stoichko Antonov ², Bader Alabbad ², Carlo U. Segre ³ and Braja K. Mandal ^{1,*}

¹ Department of Chemistry, Illinois Institute of Technology, Chicago, IL 60616, USA; zyue1@hawk.iit.edu (Z.Y.); hdunya@hawk.iit.edu (H.D.)

² Department of Mechanical, Material and Aerospace Engineering, Illinois Institute of Technology, Chicago, IL 60616, USA; mashuri@hawk.iit.edu (M.A.); santonov@hawk.iit.edu (S.A.); balabbad@hawk.iit.edu (B.A.)

³ Department of Physics & CSRRI, Illinois Institute of Technology, Chicago, IL 60616, USA; kucuk@hawk.iit.edu (K.K.); saryal@hawk.iit.edu (S.A.); segre@iit.edu (C.U.S.)

* Correspondence: mandal@iit.edu; Tel.: +1-(312)-567-3446; Fax: +1-(312)-567-3289

Received: 3 May 2020; Accepted: 6 July 2020; Published: 7 July 2020



Abstract: A new porous activated carbon (AC) material with very high specific surface area ($3193 \text{ m}^2 \text{ g}^{-1}$) was prepared by the carbonization of a colloidal silica-templated melamine–formaldehyde (MF) polymer composite followed by KOH-activation. Several electrical double-layer capacitor (EDLC) cells were fabricated using this AC as the electrode material. A number of organic solvent-based electrolyte formulations were examined to optimize the EDLC performance. Both high specific discharge capacitance of 130.5 F g^{-1} and energy density 47.9 Wh kg^{-1} were achieved for the initial cycling. The long-term cycling performance was also measured.

Keywords: electrical double-layer capacitor; porous activated carbon; specific surface area; maximum operating voltage; specific capacitance; energy density

1. Introduction

An electrical double-layer capacitor (EDLC) is an electrical energy storage device that combines the advantages of both conventional capacitors and rechargeable batteries, and offers attractive features, such as fast storing/releasing of energy, long cycling life, and high reversibility. EDLCs store energy by electrostatic absorption of ions (both cations and anions) at the interface between the electrode and electrolyte. Consequently, this process does not involve electron transfer between the electrode and electrolyte (i.e., a *non-faradic* process) [1]. This mechanism allows EDLCs to deliver much higher charging/discharging rate (usually in seconds) and longer cycling life (typically >10,000 cycles) compared to that of batteries [2–5]. However, the use of EDLC as a primary energy storage device is not practical due to their very low energy density (~one order in magnitude less than Li-ion batteries). The energy density of an EDLC cell is directly proportional to its specific capacitance (C) and the square of its maximum operating voltage (OPV) and is described by the equation: $E = \frac{1}{2} CV^2$, where V is the maximum OPV [6,7]. Since energy is stored by the accumulation of ions at the electrode-electrolyte interface, the C of EDLCs is strongly correlated with the specific surface area (SSA) of the electrodes. Accordingly, to enhance the energy density of EDLCs, it is essential to develop a porous electrode material with a very high SSA, and a matching electrolyte that can operate at a higher OPV [7]. Besides high SSA and maximum OPV, other properties of the electrode-electrolyte materials that

influence the accumulation of ions include pore diameter and pore distribution [8], dotting of hetero atoms [9], surface wettability [10] and surface roughness [11].

In the past few years, numerous carbon-based EDLC electrode materials have been reported including AC, carbon nanoparticles (CNPs) [12], carbon nanotubes (CNTs) [13,14], graphene and templated carbon [15–17]. Among these materials, porous AC materials are the most studied and the most extensively used for commercial EDLCs, because of their high electrical conductivity [18], excellent chemical/electrochemical stability, low cost, convenient preparation and abundance of precursor sources. Compared with other carbon-based materials, the supreme high SSA of AC materials has been proved by many studies, which lead to superior capacitance values. Ruoff et al. have presented the synthesis of graphene oxide (GO)-derived carbon with SSA $\sim 3100 \text{ m}^2 \text{ g}^{-1}$ by microwave treatment and KOH activation [19,20]. Niu et al. prepared carbon aerogel from resorcinol-formaldehyde (RF) activated by Na_2CO_3 and CO_2 , with SSA $3431 \text{ m}^2 \text{ g}^{-1}$ [21]. Jung et al. achieved glucose-derived foam-like graphene with SSA up to $3657 \text{ m}^2 \text{ g}^{-1}$ by both physical (CO_2) and chemical (KOH) activation [22]. By contrast, the theoretical SSAs of carbon nanotubes (CNTs) and graphene are only $1300 \text{ m}^2 \text{ g}^{-1}$ and $2630 \text{ m}^2 \text{ g}^{-1}$, respectively [16].

Liquid electrolytes for EDLCs can be classified into three major categories: aqueous-based, ionic liquid (IL)-based and organic solvent-based [6,7,23,24]. The maximum OPV of aqueous-based electrolytes is limited to $\sim 1.0 \text{ V}$ (for strong acid/base electrolytes) or $\sim 1.8 \text{ V}$ (for neutral electrolytes) due to the poor redox potential window of H_2/O_2 . Thus, despite having very high ionic conductivity ($>100 \text{ mS cm}^{-1}$), aqueous electrolyte-based EDLCs cannot deliver high energy density because of their low OPV. By contrast, IL-based electrolytes display much higher OPV (as high as $3.5\text{--}3.7 \text{ V}$) [23,25–27] but their high viscosity properties lead to low electrolyte conductivity [28,29]—a scenario not good for fast charge and discharge properties. Consequently, the current state-of-the-art electrolytes for EDLCs are organic-solvent-based, e.g., 1M tetraethylammonium tetrafluoroborate (TEA- BF_4) in acetonitrile (AN). This electrolyte displays excellent ionic conductivity (56 mS cm^{-1} [30]), which minimizes the impedance of EDLCs and enables them to be operated at very high power density. However, the maximum OPV of this electrolyte is limited to only 2.7 V , beyond which the cycling lifetime is significantly shortened. Various organic solvents, such as adiponitrile (APN) [31,32], sulfones [33] and carbonates [34], have been extensively studied for EDLC electrolytes (Table 1). Unfortunately, they typically suffer from insufficient solubility to electrolyte salts and display low ionic conductivity. Electrolytes with higher OPV with the compromise of other properties have also been developed (Table 2). Recently, DME (dimethoxyethane) has been reported as another promising solvent for EDLC electrolytes. DME possesses very low viscosity (which may significantly improve the ionic conductivity), moderate permittivity and high DN number (which provides good solubility of electrolyte salts). Jänes et al. reported an electrolyte composed of 60% of 1-ethyl-3-methyl imidazolium (EMIM- BF_4) and 40% DME (v/v)—which displayed an ionic conductivity of 24.2 mS cm^{-1} [35]. The electrochemical stability of DME is also excellent. Ruther et al. reported EDLCs based on 1M sodium hexafluorophosphate (NaPF_6) in DME electrolyte with an OPV of 3.5 V [36].

Table 1. Physical properties of commonly used organic solvents for electrical double-layer capacitor (EDLC) electrolytes.

| Solvent | Abbr. | MW ($\text{g}\cdot\text{mol}^{-1}$) | Density (g cm^{-3}) | m.p. ($^\circ\text{C}$) | b.p. ($^\circ\text{C}$) | Permittivity (25 $^\circ\text{C}$) | Viscosity (25 $^\circ\text{C}$) (cPs) | DN Number ($\text{kcal}\cdot\text{mol}^{-1}$) |
|---------------------|-------|--|-----------------------------------|---------------------------|---------------------------|-------------------------------------|--|--|
| Acetonitrile | AN | 41.05 | 0.786 | −46 | 81 | 37.5 | 0.34 | 14.1 |
| Adiponitrile | ADN | 108.14 | 0.951 | 1–3 | 295.1 | 30 [23] | 5.8 | — |
| Ethylene carbonate | EC | 88.06 | 1.321 | 34–37 | 243 | 90.5 (40 $^\circ\text{C}$) | 1.919 (40 $^\circ\text{C}$) | 16.4 |
| Dimethyl carbonate | DMC | 90.08 | 1.073 | 2–4 | 90.1 | 3.20 | 0.664 | 17.2 |
| Dimethoxy ethane | DME | 90.12 | 0.867 | −58 | 85 | 7.2 | 0.46 | 20 |
| Propylene carbonate | PC | 102.09 | 1.205 | −48.8 | 242 | 65.5 | 2.50 | 15.1 |

Table 2. Reported organic solvent-based electrolytes for the EDLCs.

| Solute | Solvent Composition | χ (25 °C) (mS cm ⁻¹) | Maximum OPV (V) | Ref. |
|---------------------------------------|--------------------------------|---------------------------------------|-----------------|------|
| 1 M LiPF ₆ | AN | 50 | 2.7 | [30] |
| 1 M TEA-BF ₄ | AN | 56 | 2.7 | |
| 1 M LiBF ₄ | AN | 18 | 2.7 | |
| 1 M LiPF ₆ | PC | 5.8 | 2.7 | |
| 1 M TEA-BF ₄ | PC | 13 | 2.7 | |
| 1 M LiBF ₄ | PC | 3.4 | 2.7 | |
| 0.7 M TEA-BF ₄ | ADN | 4.3 | 3.75 | [31] |
| 1 M SBP-BF ₄ | EiPS (ethyl isopropyl sulfone) | | 3.7 | [33] |
| 1 M LiPF ₆ | EC/DMC 1/1 v/v | ~9 | 3.2 | [34] |
| 1 M LiCF ₃ SO ₃ | EC/DMC 1/1 v/v | | Low stability | |
| 1 M NaPF ₆ | DME | 12 | 3.5 | [36] |
| 1 M NaPF ₆ | EC/PC/DMC/EA 1/1/1/0.5 v/v | ~11 | 3.4 | [37] |
| 1 M NaPF ₆ | EC/DMC | | 3.4 | [38] |
| 1 M NaClO ₄ | EC/DMC | | 3.2 | |
| 60% v/v EMIM-BF ₄ | DME 40% v/v | 24.2 | 2.7 | [35] |

In this work, we report the preparation of a new porous AC material by using MF as the precursor, and silica nanoparticles as the hard template. Our product provided a very high SSA (3193 m² g⁻¹). To identify a suitable electrolyte for this AC material, we prepared and examined the ionic conductivity of 12 formulations and fabricated EDLC coin cells with the best formulations. Several electrolytes displayed excellent capacitance with OPV up to 3.25 V.

2. Experimental

2.1. Materials

48–51 wt.% hydrofluoric (HF) aqueous solution; formaldehyde (37 wt.% aqueous solution); Starch (from potato, soluble); NaPF₆ (99+%); DME (99+%, stab. with BHT); EMIM-BF₄ (98+%); TEA-BF₄ (99%) were all purchased from Alfa Aesar. Melamine, 99+%; KOH; LP30 electrolyte (1.0 M LiPF₆ in EC/DMC = 50/50 (v/v), battery grade); EC (anhydrous, 99%) were purchased from Sigma Aldrich and used as received.

2.2. Synthesis and Characterizations of the Electrode Materials

The porous AC material for the EDLC electrodes was synthesized as follows:

Synthesis of porous carbon derived from melamine–formaldehyde (PC–MF). In a 250 mL round bottom flask, 20 mL 40 wt.% colloidal silica (~8 g SiO₂) was diluted with 100 mL DI water and then heated to ~60 °C. In a 50 mL round bottom flask, 8.4 g of melamine and 17.34 g (15.9 mL) of formaldehyde solution (37 wt.%) were mixed (molar ratio melamine/formaldehyde = 1/3.2) and heated to 80 °C with stirring. After the precursor solution became clear, heating was ceased and added to the colloidal silica suspension. Subsequently, 1 mL of acetic acid was added as the catalyst. After ~10 min, a white product was formed. The stirring and heating were continued overnight. Then, the product (SiO₂@MF) was separated by centrifuge, washed with DI water to remove any acid, and dried in an oven at 60 °C. Yield: 22.4 g.

The SiO₂@MF composite was calcined in a tube furnace under argon at 900 °C for 2 h with a heating rate of 2 °C/min. Subsequently, SiO₂ was removed by stirring in a 10 wt.% HF solution overnight. The product (PC–MF) was isolated by centrifuge, washed with DI water, and dried in an oven at 60 °C. Yield: 1.18 g.

Synthesis of porous carbon derived from starch (PC–Starch). In a 250 mL beaker, 15.0 g of soluble starch was dissolved in 60 mL DI water at 80 °C with vigorous stirring. When a transparent solution was formed, 20 mL of 40 wt.% colloidal silica dispersion was added slowly. After vigorous mechanical stirring overnight, the gel-like mixture was poured into a watch glass and allowed to cool down naturally. The jelly-like product (SiO₂@starch) was further dried at 150 °C for 24 h. Yield: 22.9 g. The subsequent carbonization and HF etching process (similar to PC–MF) produced PC–Starch. Yield: 2.81 g. Since the BET results of PC–Starch were inferior to that of PC–MF, we did not pursue the activation process (Table 3).

Table 3. BET results of new activated carbon (AC) materials.

| Carbon Precursor | Carbonization Yield from ~15 g Precursor | BET before KOH Activation | | | BET after KOH Activation | | |
|------------------|--|---------------------------------------|--|------------------------|---------------------------------------|--|------------------------|
| | | SSA (m ² g ⁻¹) | Pore Volume (cm ³ g ⁻¹) | Average Pore Size (nm) | SSA (m ² g ⁻¹) | Pore Volume (cm ³ g ⁻¹) | Average Pore Size (nm) |
| PC–Starch | 1.18 g | 676.202 | 1.679 | 12.069 | — | — | — |
| PC–MF | 2.81 g | 823.343 | 1.634 | 3.723 | 3193.395 | 3.372 | 3.535 |

Activation of PC–MF with KOH. One gram of PC–MF was thoroughly mixed with KOH (1:4 wt./wt.) manually for 30 min in a mortar. The mixture was transferred to an Al₂O₃ boat and heated in a tube furnace at 800 °C for 2 h under Ar flow, with a heating rate of 5 °C/min. The product was washed with DI water and refluxed in 1 M HCl solution overnight to remove all base and metal ions. The KOH-activated porous AC product (PC–KOH) was washed with DI water until the filtrate was neutral. Finally, the product was dried in an oven at 60 °C. Yield: ~216 mg.

BET and SEM characterizations. The BET measurements, as shown in Table 3, for PC–MF, PC–Starch, and PC–KOH were carried out with a two-channel Nova Quantachrome® 2200e surface area & pore size analyzer. SEM images were taken in a JEOL JSM5900LV (JEOL Ltd., Tokyo, Japan) scanning electron microscope.

2.3. Formulations of the Electrolytes and Ionic Conductivity Measurement

As depicted in Table 4, we have prepared 12 electrolyte formulations with various salt-solution compositions. Their ionic conductivities were measured by a Mettler Toledo S230-Kit conductivity meter in an environmental chamber set at 25 °C [39]. The calibration of the conductivity meter was performed using a standard (aqueous 0.01 mol L⁻¹ KCl solution with an ionic conductivity of 1.314 mS cm⁻¹ at 25 °C).

Table 4. Conductivity of the electrolyte formulations designed in this study.

| Electrolyte | χ (25 °C) (mS cm ⁻¹) ^a | Our Measurement | Literature |
|-------------|--|-------------------|------------|
| #1 | EMIM–BF ₄ /DME = 6/4 | 24.7 | 24.2 |
| #2 | EMIM–BF ₄ /DME = 4/6 | Not miscible | |
| #3 | EMIM–BF ₄ /EC/DME = 4/1/5 | 25.8 | |
| #4 | EMIM–BF ₄ /EC/DME = 4/3/3 | 26.8 | |
| #5 | 1M TEA–BF ₄ in DME | Not miscible | |
| #6 | 1M TEA–BF ₄ in EC/DME = 1/4 | Not miscible | |
| #7 | 1M TEA–BF ₄ in EC/DME = 1/1 | 13.7 | |
| #8 | 1M LiPF ₆ in EC/DMC = 1/1 (LP30) | Commercial sample | ~9 |
| #9 | 1M NaBF ₄ in EC/DME = 1/1 | Not miscible | |
| #10 | 1M NaPF ₆ in DME | 12.8 | |
| #11 | 1M NaPF ₆ in EC/DME = 1/4 | 16.6 | |
| #12 | 1M NaPF ₆ in EC/DME = 1/1 | 12.3 | |

^a All solvents are in volume ratio.

2.4. Fabrication of EDLC Coin Cells

Fabrication of coin cells. First, an electrode slurry was prepared by mixing 90 wt.% PC-KOH and 10 wt.% carboxymethyl cellulose (CMC) binder in a water/ethanol (1:1) solution. Second, a thin film of the slurry was casted over an aluminum foil using a doctor blade and then dried at 60 °C for 24 h. Third, the AC-coated aluminum foil was punched to obtain electrode discs. Each disc contained ~1.8 mg (± 0.1 mg) of the composite electrode material. Finally, CR2032-type coin cells were assembled in an Ar-filled glove box with oxygen content less than 1 ppm. The cells were symmetric with Celgard 2535 as the separator.

2.5. Electrochemical Measurements

Cyclic voltammetry (CV). CV scans were performed using a PARSTAT 4000A Potentiostat Galvanostat instrument. Two-electrode test cells were initially charged from the open circuit voltage to the maximum voltage (2.50 V to 3.50 V with a gradual increase of 0.25 V per test run). Subsequently, the voltage was scanned between 0 and maximum at a scan rate of 10 mV s⁻¹.

Electrochemical impedance spectroscopy (EIS). EIS data were collected with the above instrument in the frequency range of 0.1 MHz to 1 Hz with a potential amplitude of 10 mV.

Cycling performance. The cycling performance of the cell was investigated using an MTI battery analyzer (BST8-WA). Initially, we performed 50 charge–discharge cycles with different formulations at current density of 0.5, 1.0, 2.0, and 4.0 A g⁻¹ and then a long-term (4000 cycles) cycling test with the best two electrolytes.

3. Results and Discussion

3.1. Synthesis and Properties of the Electrode Material

A new porous AC material was synthesized by using MF as the precursor and silica nanoparticles as the hard template. We also attempt to apply the same method but using a natural polymeric material precursor, such as corn starch, as an alternative carbon source. The advantage of starch over MF is that we could skip the polymerization process. However, in practice this is a time-consuming process and difficult to apply for the production in large scale with the apparatus available in our lab. The jelly-like SiO₂@starch became a stone-like hard material, which is very difficult to blend with KOH. After calcination and HF etching, the porous AC material derived from MF (PC-MF) and starch (PC-Starch) were characterized by BET. The results are depicted in Figure 1 and Table 3. As shown in Table 3, both porous carbon materials displayed high SSA and excellent pore volume. The carbonization process resulted in high yield for PC-Starch (about two times higher than that of PC-MF). However, PC-MF displayed much higher SSA, while the average pore size of PC-starch is much larger (12.07 nm vs. 3.72 nm), and the size distribution is also narrower.

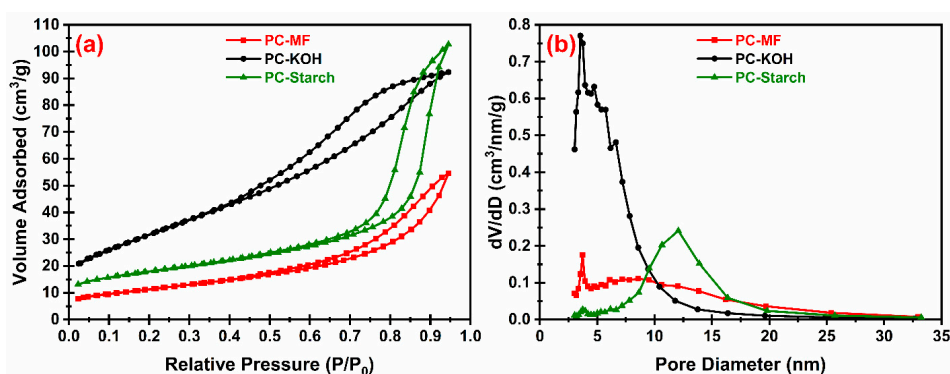


Figure 1. (a) Nitrogen adsorption-desorption isotherm curves and (b) pore size distribution of PC-MF, PC-KOH, and PC-Starch.

To further increase SSA, KOH activation was applied to the PC-MF material. The KOH/carbon ratio during activation significantly influences the properties of the carbon material. Lu et al. compared the different activation results by using KOH:carbon ratios of 1:2, 1:4 and 1:5. They showed that much superior SSA and mesoporous pore volume can be obtained when the ratio equals 1:4 [40]. In the recent past, AC materials with high SSA have been prepared by KOH activation using a variety of carbon precursors, viz., pollen [41], wood powder [42] and other biomasses [43]. The KOH activation process has been reported to give the highest SSA among all reported methods, viz., surface treatment with steam, CO or CO₂, and chemical activation with ZnCl₂, Na₂CO₃ and phosphoric acid. Although the KOH activation has been widely used, the activation mechanism is not well understood. The reaction includes multiple steps and is very complicated. In general, potassium ions are reduced to metallic potassium and carbon is partially oxidized to CO or CO₂, which create pores and voids in the carbon matrix, leading to significant increase in SSA [44]. Most of these studies used a KOH:carbon ratio of 1:4. It is important to note that ~80% of the mass of carbon is lost during the KOH activation process. On the positive side, it is an excellent method for obtaining very high SSA materials (3293 m² g⁻¹). Remarkably, the pore volume was also increased by ~106%.

The SEM images display the morphology changes of the porous carbon material before and after the KOH activation process (Figure 2). Clearly, both of them are highly porous materials. However, visually PC-MF is an amorphous structure containing many pores with diameter >50 nm (Figure 2a,d), but after the KOH activation these pores have collapsed—only diameters <20 nm can be seen in Figure 3d. We believe that the multilayer structure of KOH activated PC-MF is possibly due to the formation of graphitic carbon (Figure 2c).

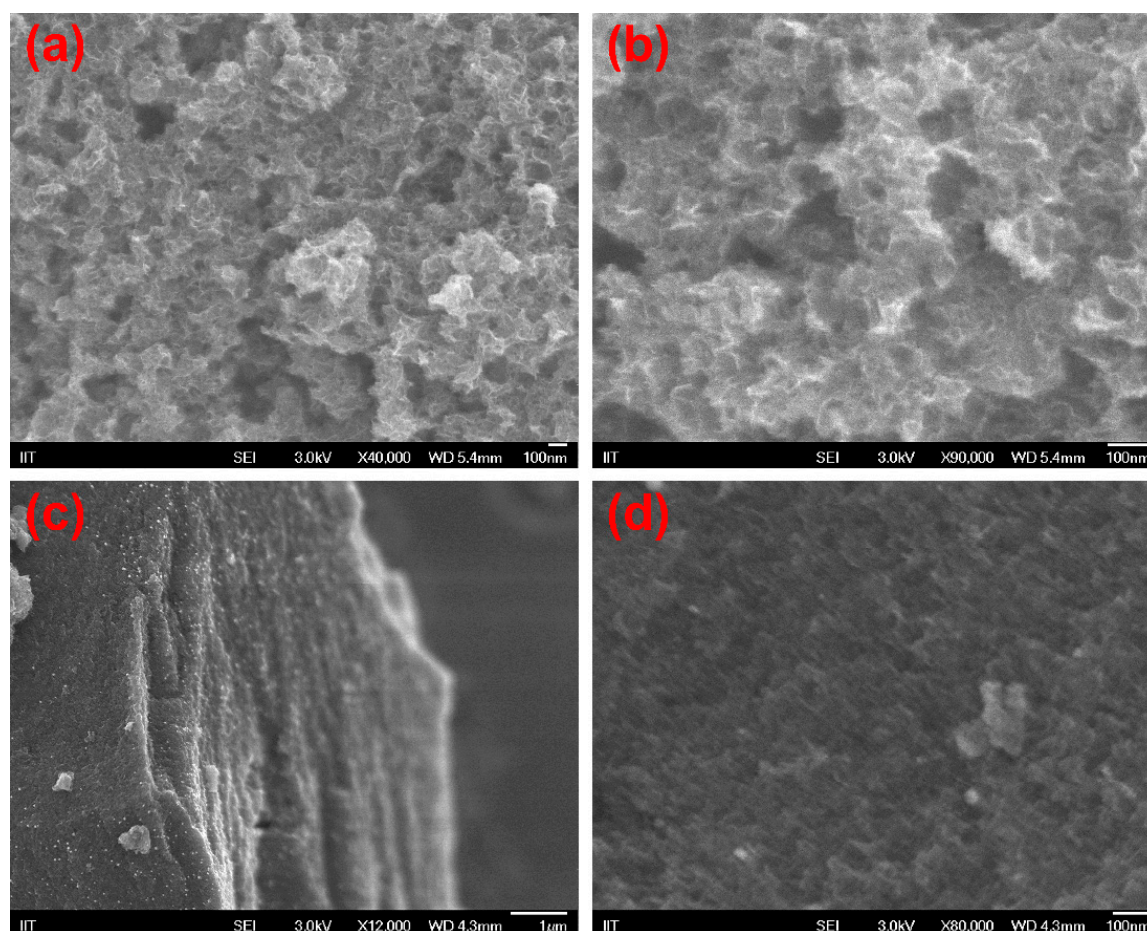


Figure 2. Scanning electron microscopy (SEM) images of PC-MF and PC-KOH. (a) PC-MF, (b) PC-MF, (c) PC-KOH, and (d) PC-KOH.

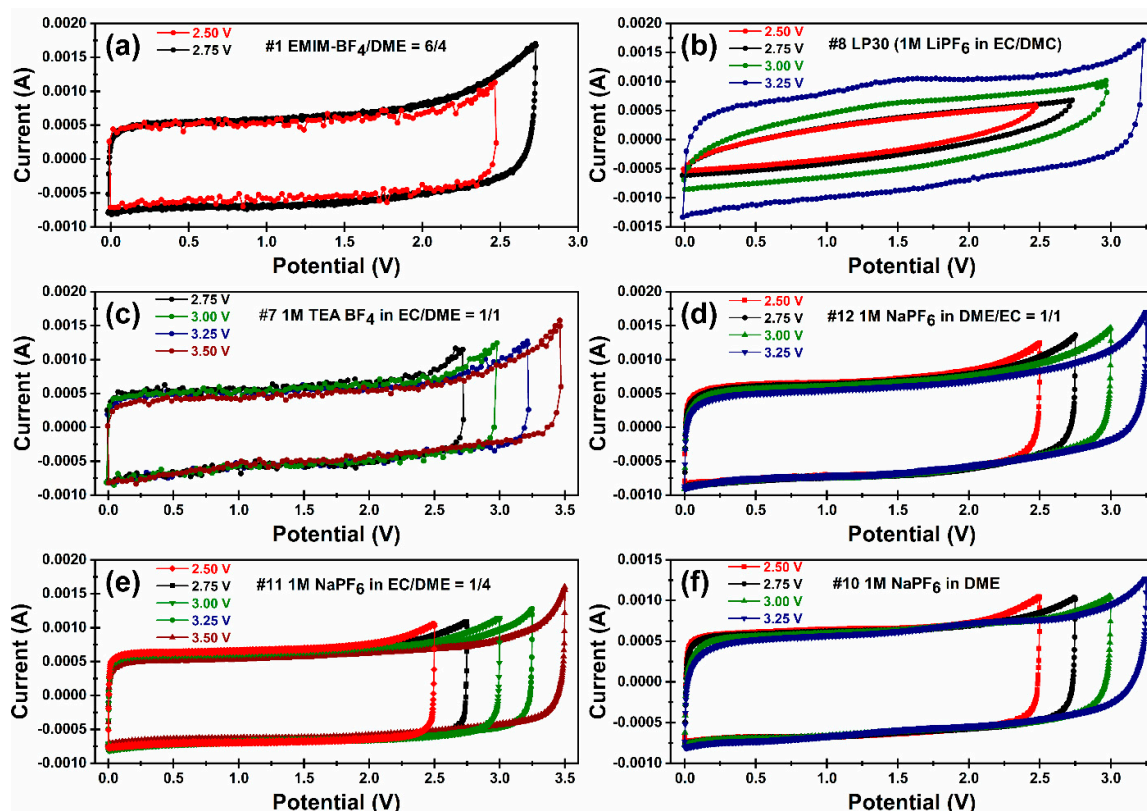


Figure 3. Cycling voltammety curves of EDLC cells with formulations (a) #1, EMIM–BF₄/DME = 6/4 v/v; (b) #8, LP30 (1 M LiPF₆ in EC/DMC = 1/1 v/v); (c) #7, 1 M TEA–BF₄ in EC/DME = 1/1 v/v; (d) #12, 1 M NaPF₆ in EC/DME = 1/1 v/v; (e) #11, 1 M NaPF₆ in EC/DME = 1/4 v/v; (f) #10, 1 M NaPF₆ in DME.

3.2. Electrolyte Formulations

In EDLC devices, an electrolyte not only influences the maximum OPV but also the specific capacitance of the cell. It is very important that the electrolyte be closely matched with the properties of the AC (viz., surface area, pore volume and pore diameter). High surface area allows more absorptions of ions, while pore volume facilitates electrolyte penetration in the AC (solvent reservoir). If the AC possesses more micropores (pore diameter <2 nm), the sizes of cation and anion species and the ion-solvent interaction become relevant [28]. BF₄[−] has been the best choice to increase the specific capacitance because of its small size, which permits more anions to accumulate per unit surface area [28]. Additionally, small ions can penetrate to small pores on the electrode surface [45]. Most importantly, ILs containing BF₄[−] usually display higher electrochemical stability and ionic conductivity than other widely used anions, such as TFSI[−] and PF₆[−] [23,28]. However, because of their higher lattice energy, typically the solubility of BF₄[−]-based ILs in organic solvents is comparatively lower, and for the same reason the ionic conductivity of LiBF₄ solution is poor (Table 1). Mousavi et al. also observed poor wettability of EMIM–BF₄ with the mesoporous carbon model electrodes [28], leading to poor overall EDLC performance.

Although inorganic cations, such as Li⁺ and Na⁺, have dimensions that are much smaller than organic cations like TEA⁺ or EMIM⁺, the kinetics of their adsorption/desorption process is sluggish because of a strong solvation effect. Theoretical simulation and experimental characterization studies have indicated that solvation ion clusters, such as Li⁺(EC)₂ or Li⁺(EC)₃ complexes are the main cationic species in solutions made of polar organic solvents [46]. By contrast, in the “soft” organic cations, the charge is effectively distributed/shielded and the interaction with the solvent molecules is much weaker. As shown in Table 1, TEA–BF₄ in organic solution displayed much higher conductivity than Li⁺/Na⁺ salt-based formulations. However, the advantage of Li⁺/Na⁺ is that they have no redox stability concerns.

As mentioned earlier, organic solvents for EDLCs must possess high electrochemical stability. A good solvent system should also offer (a) low viscosity, which typically leads to high ionic conductivity; (b) high donor number, which indicates the ability of a solvent to solvate cations; and (c) high permittivity, which increases the dissociation of the solute cations/anions. Based on this understanding, we prepared several electrolyte formulations listed in Table 4.

As shown in Table 2, EC possesses high permittivity and donor number, which means EC can readily dissolve high lattice energy salts and improve ionic conductivity by creating better cation/anion dissociation. Furthermore, previous reports have demonstrated its electrochemical stability window (ESW) of at least ~3.2 V when combined with other carbonate solvents [34,47,48]. However, EC has a melting point slightly higher than room temperature, and comparatively high viscosity; which calls for a “thinner” co-solvent. We decided to use DME instead of most popular low viscosity carbonates (PC/DMC) because of its high donor number, low viscosity, low m.p. and excellent ESW—which could compensate the drawbacks of EC.

The ionic conductivity results met our expectations very well. The properties of solutions #2, #3 and #4 proved that a small proportion of EC could enhance the solubility of EMIM-BF₄; while a higher proportion of EC leads to slightly better conductivity. During the preparation of solutions #5, #6 and #7 we noticed that EC facilitates the solubility of TEA-BF₄. The electrolyte #11 (which contains 20% EC) showed much higher conductivity than #12 (pure DME), but when the ratio of EC was increased to 50%, the conductivity of #13 dropped, possibly because of the enhancement of solution viscosity. Accordingly, we selected formulations #1, #7, #8, #10, #11 and #12 as the electrolytes for our EDLC experiments.

3.3. Electrochemical Performance

Cyclic voltammetry measurements. The maximum OPV of an EDLC coin cell is best determined by the CV experiment. We started scanning from 0–2.5 V, and then gradually increased the upper limit of OPV, until unwanted redox peaks appeared at the high potential (the “sharp peak”). This is typically due to the oxidation reaction on the anode with concurrent reduction of the electrolyte, and/or the reduction reaction on the cathode with simultaneous oxidation in the electrolyte. This CV study allows us to determine the approximate range of the maximum OPV. The results can be summarized as follows: the maximum OPV was between 2.50–2.75 V for EMIM-BF₄/DME = 6/4 (#1); 3.0–3.25 V for 1M LiPF₆ in EC/DME = 1/1 (#8); 3.25–3.50 V for TEA-BF₄ in EC/DME (#7); 3.0–3.25 V for 1M NaPF₆ in DME (#10); 3.0–3.25 V for 1M NaPF₆ in DME/EC = 4/1 (#11) and 2.75–3.0 V for 1M NaPF₆ in DME/EC = 1/1 (#12). When scanned at voltage lower than that of maximum OPV, the CV curves were rectangular shape, showing behavior of EDLC system was nearly ideal capacitive. At cell potentials exceeding the maximum OPV, an exponential increase in current density occurs. This may be due to the adsorption of Li⁺ and partial charge transfer at negatively charged carbon electrode. The oxidation of surface functionalities at the positively charged carbon electrode cannot be ruled out [49]. The abnormal bump in Figure 3b may response to the reduction of trace H₂O present in the electrolyte.

As can be seen from Figure 3a, the ESW of #1 is much narrower compared to the other formulations. This might be due to poor electrochemical stability of EMIM⁺, which possesses an acidic hydrogen atom at 2-position. The electrolyte #7 displayed the best ESW (i.e., high electrochemical stability of both the cation and anion) among all formulations we studied. Several research groups have reported similar electrochemical stability of electrolytes containing BF₄[−] rather than PF₆[−] [50].

By comparing the CV curves for samples #10, #11 and #12 (Figure 3d–f), we could see the “sharp peaks” appearing at lower voltages when more EC was added. This indicates that a higher ratio of EC lowers the electrochemical stability of the electrolytes. Previous research studies [23,28,50] also observed this behavior and proposed that the H-transfer reaction between fluorinated anions (PF₆[−], BF₄[−] and FSI[−]) and carbonate solvents is responsible for marked decrease the oxidative stability.

Electrochemical impedance spectroscopy (EIS). The inner resistance of the EDLC cells can be determined from the EIS and the Nyquist plots (Figure 4). Several confusing and often contradictory

explanations to the Nyquist plots of EDLC have been proposed in the literature. We agree with the explanation provided by Mei et al. [51]. The starting point of a Nyquist plot curve represents the bulk electrolyte resistance R_A ; the semicircle at high frequency region represents the so-called charge-transfer resistance R_B (so that the internal resistance equals $R_A + R_B$); and the vertical line at low frequencies was attributed to the capacitive behavior of the EDLC. According to this theory, the cell with electrolyte #1 displayed the lowest internal resistance ($\sim 1.6 \Omega$) and an extremely small semicircle (Figure 4a). The cells with electrolytes #7, #10, #11 and #12 have slightly larger internal resistance than #1, and the size of their semicircles are all at the same level (Figure 4b). When comparing electrolytes #10, #11 and #12, we can see the addition of EC decreased the bulk electrolyte resistance (R_A), which is consistent with our ionic conductivity measurement. However, the diameter of the semicircles (R_B) are much larger, as a result, the internal resistance is even higher, which is possibly caused by the stronger solvation effect, because EC has more polarity than DME. The EIS curve of the electrolyte #7 (1 M TEA-BF₄ in EC/DME = 1/1) shows a much smaller semicircle than the electrolyte #12 (1 M NaPF₆ in EC/DME = 1/1). This can be explained by the better charge-transfer kinetics, possibly caused by the smaller size of BF₄⁻ than PF₆⁻ and lesser solvation effect of TEA⁺ than Na⁺, so that the transport of ions between electrolyte and the pores on the electrode surface becomes faster. Only one semicircle curve was obtained for the electrolyte #7, while multiple semicircles were observed for electrolytes #10, #11 and #12. This is indicative of different charge-transfer processes of the solvated ions. Other groups have also noticed similar high charge-transfer resistance behavior, indicating a hindrance in transferring charge at the interface [52–54]. This may be due to a combination of many factors, viz. (i) poor contact between the active material and current collector, (ii) high ionic resistance of the electrolyte and high intrinsic resistance of the active material and (iii) high resistance of the movement of ions at the electrode/electrolyte interface.

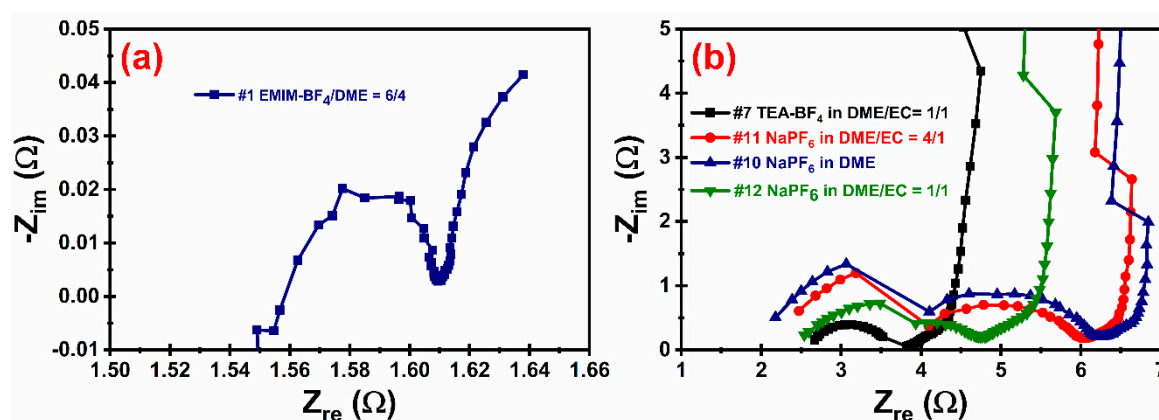


Figure 4. Electrochemical impedance spectroscopy (EIS) of coin cells with different electrolytes. (a) EMIM-BF₄/DME = 6/4 and (b) 1 M TEA-BF₄ EC/DME = 1/1, 1 M NaPF₆ in DME, 1 M NaPF₆ in DME/EC = 4/1, and 1 M NaPF₆ in DME/EC = 1/1.

Cycling performance of EDLC cells. The cycling performance of the EDLC cells was determined using an MTI battery analyzer (BST8-WA). Several coin cells were prepared with six different electrolyte formulations. Their charging-discharging cycles were recorded at different current densities: 0.5, 1.0, 2.0 and 4.0 A g⁻¹. Figure 5 depicts the initial charging/discharging curves for all electrolytes. Specific capacitance and energy density values were calculated based on the initial (50th) cycle discharging time and OPV. The results are summarized in Table 5. The Coulombic efficiency (C_d/C_c) of the EDLC cells was determined from the ratio of discharging/charging time of the displayed cycle at 1 A g⁻¹. It is noteworthy that although the electrolyte #1 has the lowest internal resistance and possesses a very good C value, this system displayed the lowest E among all six formulations due to the low OPV. For the electrolyte #8, the cell displayed the higher C and E than that of electrolytes #1 and #7, despite a high OPV of the electrolyte #7. This may be due to the larger C caused by the small size of Li⁺

compared to the organic cations, which allows more ion stacking at the electrode-electrolyte interface. However, the huge internal resistance leads to the low coulombic efficiency of the cell, which means a considerable loss of electrical energy. Under a constant current, the integral of voltage with respect to time equals the electrical energy. As shown in Figure 5b, the low energy storage efficiency of cell containing the electrolyte #8 is illustrated by the great difference between the area under the charging curve and that under the discharging curve, which is much more severe than cells based on the other electrolytes.

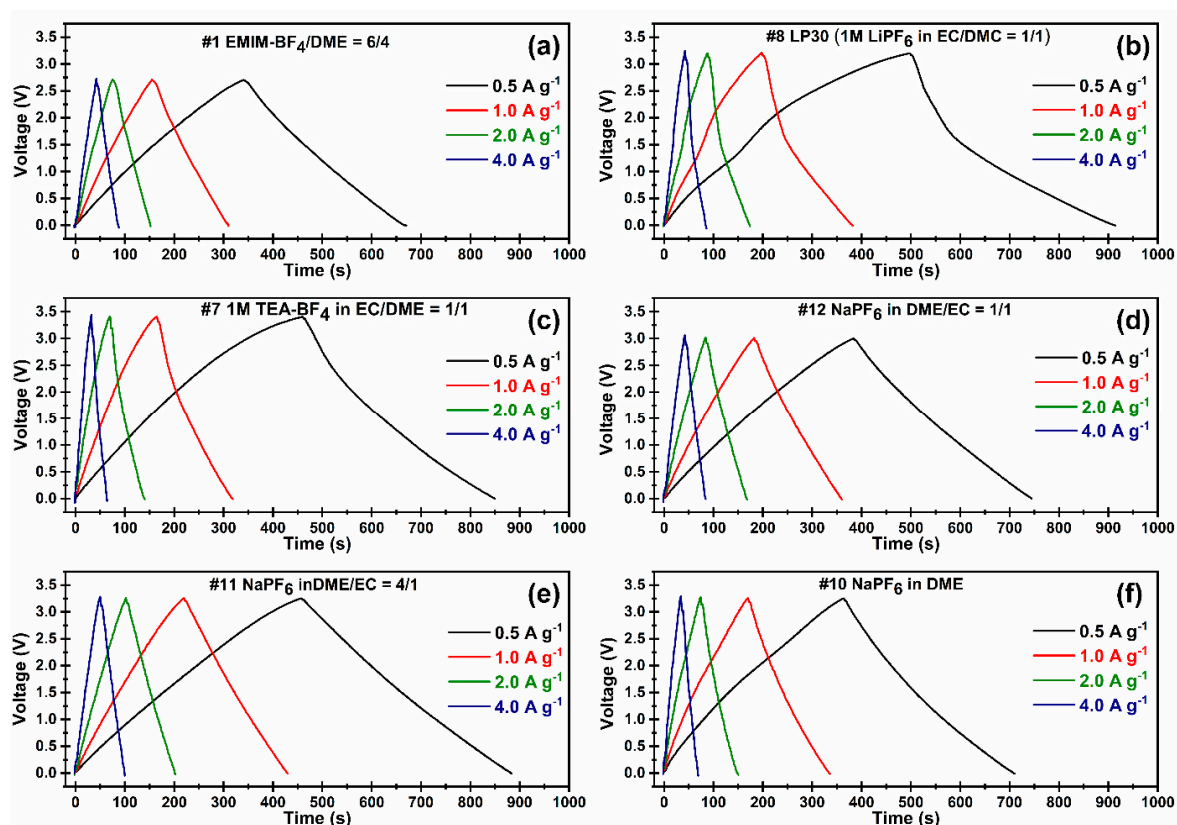


Figure 5. The initial charging–discharging curves at different current rates of EDLCs with electrolytes (a) #1, EMIM–BF₄/DME = 6/4 v/v, (b) #8, 1 M LiPF₆ in EC/DMC = 1/1 v/v (LP30), (c) #7, 1 M TEA–BF₄ in EC/DME = 1/1 v/v, (d) #12, 1 M NaPF₆ in DME/EC = 1/1 v/v, (e) #11, 1 M NaPF₆ in DME/EC = 4/1 v/v, and (f) #10, 1 M NaPF₆ in DME.

Table 5. Summary of the electrochemical properties of the EDLC cells with different electrolyte formulations.

| | #1 | #7 | #8 | #10 | #11 | #12 |
|--|-------------------------------------|---|--|------------------------------|---|---|
| Electrolyte formulation | EMIM-BF ₄ /DME = 6/4 v/v | 1 M TEA-BF ₄ in EC/DME = 1/1 v/v | 1 M LiPF ₆ in EC/DMC = 1/1 v/v (LP30) | 1 M NaPF ₆ in DME | 1 M NaPF ₆ in EC/DME = 1/4 v/v | 1 M NaPF ₆ in EC/DME = 1/1 v/v |
| Maximum OPV, (V) | 2.5–2.75 | 3.25–3.5 | 3.0–3.25 | 3.0–3.25 | 3.0–3.25 | 2.75–3.0 |
| Internal resistance, (Ohm) | ~1.6 | ~3.7 | ~620 | ~4.6 | ~5.9 | ~6.1 |
| Coulombic efficiency ^a C _d /C _c (%) | 96.5 | 92.2 | 91.9 | 97.1 | 95.4 | 97.3 |
| Initial specific discharge capacitance ^a , C (F g ⁻¹) | 112.7 | 87.9 | 113.2 | 102.8 | 130.5 | 119.0 |
| Initial energy density ^a , E (Wh kg ⁻¹) | 29.6 | 37.4 | 46.0 | 34.8 | 47.9 | 37.2 |

^a Data of the 50th cycle. Calculated at the current density of 1 A g⁻¹.

In contrast, the cell with the electrolyte #7 can sustain the highest OPV, although C is the lowest among all six formulations, because of the larger size and sphere-like shape of TEA^+ . The planar-shape of EMIM cation may lead to higher C (electrolyte #1). This cell also suffered a comparatively low energy storage efficiency. To conclude, the electrolytes #10, #11 and #12 are found to be the best electrolytes in this study, especially, the electrolyte #11, which attained the highest C and E , while recording a Coulombic efficiency $>95\%$.

Long-term cycling performance. Two electrolyte formulations with the best comprehensive performance (#11, 1 M NaPF_6 in EC/DME = 1/4 v/v and #10, 1 M NaPF_6 in DME) were selected for the long-term cycling test. These EDLC cells were cycled at a current density of 1.0 A g^{-1} and OPV 0~3.25 V for 4000 cycles, and their specific discharge capacitance were recorded (Figure 6).

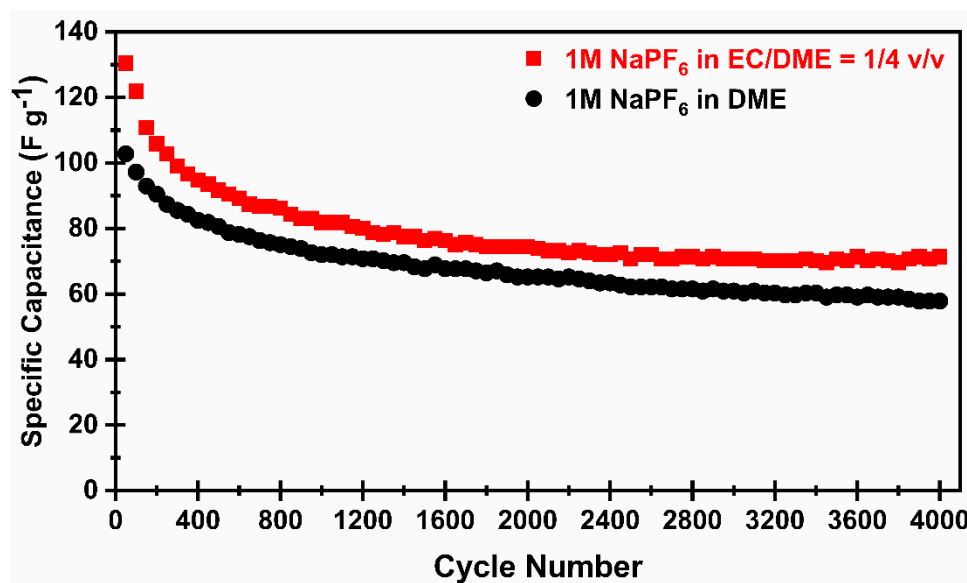


Figure 6. Long-term cycling performance of the KOH activated PC–MF electrode in electrolytes #10 and #11 at a current density of 1.0 A g^{-1} and OPV 0–3.25 V.

It is a common observation that supercapacitor cells made of active carbon and organic electrolytes experience performance fading in the first 1500 cycles. This is a result of both decrease in capacitance and increase in equivalent series resistance (ESR) [55–59]. The capacitance fading is believed to be driven by two mechanisms. The first one is associated with the exponential function of square root of time of ageing, while the second one is described by the Gaussian function. The first ageing mechanism (presumably related to the degradation of electrolytes) is observed for most samples, while the second mechanism is significant only under harsh testing conditions, such as elevated temperature and/or increased operating voltage. The degradation rate due to the cycling ageing test is much higher than the degradation rate due to the calendar ageing test with equivalent voltage and temperature [60–62]. We presume that the second ageing mechanism is related to the electrode active area degradation caused probably by the decrease of potential barrier on the electrode/electrolyte interface.

As expected, both cells experienced fast capacitance decay in the first 1500 cycles, but after that the decay rate became very minimal. For the next 2500 cycles, the specific capacitance retention of both EDLC cells were 93.6% and 85.4%, respectively (Table 6). For the cell with 1M NaPF_6 in EC/DME = 1/4 v/v electrolyte, after 4000 cycles, its specific capacitance and energy density were calculated at 71.4 F g^{-1} and 26.2 Wh kg^{-1} , respectively. These results are superior to most reported organic solvent-based EDLCs [63–65]. Similar phenomena have been reported in the EDLC research of Väli et al. using NaPF_6 in EC/DMC/PC/EA = 1/1/1/0.5 (volume ratio) as the electrolyte [37]. Since the specific discharging capacitance was still very high and kept stable after long-term cycling, we believe the fast capacitance fading during the first 1500 cycles was not caused by the blocking of the micro pores or the passivation

of the electrode surfaces. We believe a part of the reasons may be due to the high contribution of pseudocapacitance created by the N and O functionalities on the electrode surface, which has been widely researched in symmetric supercapacitors based on KOH-activated N-doped carbon electrodes and aqueous electrolytes [65,66]. This type of N-doped carbon electrode material could be prepared by calcination of MF or other nitrogen-containing precursors [63,64,67]. The maximum OPV of aqueous-electrolyte supercapacitors are usually ~1.0 V (strong-acid/base) or ~1.8 V (neutral). However, in our experiments under higher OPV these N and O functionalities may experience slow oxidation/reduction, leading to the decay of pseudocapacitance.

Table 6. Specific discharge capacitance retention of the KOH activated PC–MF electrode with electrolytes #10 and #11 after 4000 cycles.

| Electrolyte Formulation | Initial (50th) C_d (F g ⁻¹) | 1500th C_d (F g ⁻¹) | C_d Retention of the First 1500 Cycles (%) | 4000th C_d (F g ⁻¹) | C_d Retention of the Next 2500 Cycles (%) |
|---|---|-----------------------------------|--|-----------------------------------|---|
| 1 M NaPF ₆ in DME (#10) | 102.8 | 67.7 | 65.9% | 57.8 | 85.4% |
| 1 M NaPF ₆ in EC/DME = 1/4 v/v (#11) | 130.5 | 76.3 | 58.5% | 71.4 | 93.6% |

4. Conclusions

By virtue of the equation $E = \frac{1}{2} CV^2$, a high SSA carbon material that could provide more area for ion stacking, and a matching electrolyte that could support high operation voltage is necessary for achieving high energy density. We successfully prepared a very high SSA porous carbon material from MF followed by KOH-activation. The AC material displayed an SSA of 3193 m² g⁻¹. To identify an electrolyte formulation with the best comprehensive property, 12 formulations were prepared, and their ionic conductivities were measured. The electrochemical performance of coin cells composed of carbon electrode and six best electrolyte formulations were evaluated. With 1 M NaPF₆ in EC/DME = 1/4 v/v electrolyte, our cells could support an operation voltage up to 3.25 V, which resulted in high specific capacitance (130.5 F g⁻¹) and high energy density (47.9 Wh kg⁻¹). Long-term cycling stability was also good after 4000 cycles.

Author Contributions: Z.Y. (Conceptualization, Methodology, Investigation, Writing original draft); H.D. (Software, Methodology, Data curation); M.A. (Data curation, Investigation, Writing, review & editing); K.K. (Writing, Investigation, Data curation, Visualization); S.A. (Shankar Aryal) (Software, Review & editing, Data curation); S.A. (Stoichko Antonov) (Investigation, Data curation); B.A. (Investigation, Data curation); C.U.S. (Supervision, Writing, review & editing); B.K.M. (Conceptualization, Methodology, Supervision, Writing, review & editing). All authors have read and agreed to the published version of the manuscript.

Funding: We thank the Wanger Institute for Sustainable Energy Research (WISER# 6-1-17) Foundation for the partial financial support of this research work.

Conflicts of Interest: The authors declare no conflict of interest.

References

1. Suda, Y.; Mizutani, A.; Harigai, T.; Takikawa, H.; Ue, H.; Umeda, Y. Influences of internal resistance and specific surface area of electrode materials on characteristics of electric double layer capacitors. *AIP Conf. Proc.* **2017**, *1807*, 020022. [[CrossRef](#)]
2. Simon, P.; Gogotsi, Y.; Dunn, B. Where Do Batteries End and Supercapacitors Begin? *Science* **2014**, *343*, 1210–1211. [[CrossRef](#)] [[PubMed](#)]
3. Choi, N.-S.; Chen, Z.; Freunberger, S.A.; Ji, X.; Sun, Y.-K.; Amine, K.; Yushin, G.; Nazar, L.F.; Cho, J.; Bruce, P.G. Challenges Facing Lithium Batteries and Electrical Double-Layer Capacitors. *Angew. Chem. Int. Ed.* **2012**, *51*, 9994–10024. [[CrossRef](#)] [[PubMed](#)]
4. Gu, W.; Yushin, G. Review of nanostructured carbon materials for electrochemical capacitor applications: Advantages and limitations of activated carbon, carbide-derived carbon, zeolite-templated carbon, carbon aerogels, carbon nanotubes, onion-like carbon, and graphene. *WIREs Energy Environ.* **2014**, *3*, 424–473. [[CrossRef](#)]

5. González, A.; Goikolea, E.; Barrena, J.A.; Mysyk, R. Review on supercapacitors: Technologies and materials. *Renew. Sustain. Energy Rev.* **2016**, *58*, 1189–1206. [[CrossRef](#)]
6. Zhong, C.; Deng, Y.; Hu, W.; Qiao, J.; Zhang, L.; Zhang, J. A review of electrolyte materials and compositions for electrochemical supercapacitors. *Chem. Soc. Rev.* **2015**, *44*, 7484–7539. [[CrossRef](#)]
7. Wu, Z.; Li, L.; Yan, J.-m.; Zhang, X.-b. Materials Design and System Construction for Conventional and New-Concept Supercapacitors. *Adv. Sci.* **2017**, *4*, 1600382. [[CrossRef](#)] [[PubMed](#)]
8. Chmiola, J.; Yushin, G.; Gogotsi, Y.; Portet, C.; Simon, P.; Taberna, P.L. Anomalous Increase in Carbon Capacitance at Pore Sizes Less Than 1 Nanometer. *Science* **2006**, *313*, 1760–1763. [[CrossRef](#)]
9. Bo, Z.; Li, C.; Yang, H.; Ostrikov, K.; Yan, J.; Cen, K. Design of Supercapacitor Electrodes Using Molecular Dynamics Simulations. *Nano-Micro Lett.* **2018**, *10*, 33. [[CrossRef](#)]
10. Yang, H.; Bo, Z.; Yan, J.; Cen, K. Influence of wettability on the electrolyte electrosorption within graphene-like nonconfined and confined space. *Int. J. Heat Mass Transf.* **2019**, *133*, 416–425. [[CrossRef](#)]
11. Yang, H.; Zhang, X.; Yang, J.; Bo, Z.; Hu, M.; Yan, J.; Cen, K. Molecular Origin of Electric Double-Layer Capacitance at Multilayer Graphene Edges. *J. Phys. Chem. Lett.* **2017**, *8*, 153–160. [[CrossRef](#)] [[PubMed](#)]
12. Yang, Y.; Shen, K.; Liu, Y.; Tan, Y.; Zhao, X.; Wu, J.; Niu, X.; Ran, F. Novel Hybrid Nanoparticles of Vanadium Nitride/Porous Carbon as an Anode Material for Symmetrical Supercapacitor. *Nano-Micro Lett.* **2016**, *9*, 6. [[CrossRef](#)] [[PubMed](#)]
13. Zhao, J.; Zhang, Y.; Huang, Y.; Xie, J.; Zhao, X.; Li, C.; Qu, J.; Zhang, Q.; Sun, J.; He, B.; et al. 3D Printing Fiber Electrodes for an All-Fiber Integrated Electronic Device via Hybridization of an Asymmetric Supercapacitor and a Temperature Sensor. *Adv. Sci.* **2018**, *5*, 1801114. [[CrossRef](#)] [[PubMed](#)]
14. Wang, L.; Zhang, G.; Zhang, X.; Shi, H.; Zeng, W.; Zhang, H.; Liu, Q.; Li, C.; Liu, Q.; Duan, H. Porous ultrathin carbon nanobubbles formed carbon nanofiber webs for high-performance flexible supercapacitors. *J. Mater. Chem. A* **2017**, *5*, 14801–14810. [[CrossRef](#)]
15. Zhang, F.; Liu, T.; Li, M.; Yu, M.; Luo, Y.; Tong, Y.; Li, Y. Multiscale Pore Network Boosts Capacitance of Carbon Electrodes for Ultrafast Charging. *Nano Lett.* **2017**, *17*, 3097–3104. [[CrossRef](#)]
16. Yang, Z.; Tian, J.; Yin, Z.; Cui, C.; Qian, W.; Wei, F. Carbon nanotube- and graphene-based nanomaterials and applications in high-voltage supercapacitor: A review. *Carbon* **2019**, *141*, 467–480. [[CrossRef](#)]
17. Han, Y.; Lai, Z.; Wang, Z.; Yu, M.; Tong, Y.; Lu, X. Designing Carbon Based Supercapacitors with High Energy Density: A Summary of Recent Progress. *Chem. Eur. J.* **2018**, *24*, 7312–7329. [[CrossRef](#)]
18. Yang, W.; Yang, W.; Ding, F.; Sang, L.; Ma, Z.; Shao, G. Template-free synthesis of ultrathin porous carbon shell with excellent conductivity for high-rate supercapacitors. *Carbon* **2017**, *111*, 419–427. [[CrossRef](#)]
19. Zhu, Y.; Murali, S.; Stoller, M.D.; Velamakanni, A.; Piner, R.D.; Ruoff, R.S. Microwave assisted exfoliation and reduction of graphite oxide for ultracapacitors. *Carbon* **2010**, *48*, 2118–2122. [[CrossRef](#)]
20. Zhu, Y.; Murali, S.; Stoller, M.D.; Ganesh, K.J.; Cai, W.; Ferreira, P.J.; Pirkle, A.; Wallace, R.M.; Cychosz, K.A.; Thommes, M.; et al. Carbon-Based Supercapacitors Produced by Activation of Graphene. *Science* **2011**, *332*, 1537–1541. [[CrossRef](#)]
21. Liu, N.; Shen, J.; Liu, D. Activated high specific surface area carbon aerogels for EDLCs. *Microporous Mesoporous Mater.* **2013**, *167*, 176–181. [[CrossRef](#)]
22. Jung, S.; Myung, Y.; Kim, B.N.; Kim, I.G.; You, I.-K.; Kim, T. Activated Biomass-derived Graphene-based Carbons for Supercapacitors with High Energy and Power Density. *Sci. Rep.* **2018**, *8*, 1915. [[CrossRef](#)] [[PubMed](#)]
23. Lewandowski, A.; Olejniczak, A.; Galinski, M.; Stepniak, I. Performance of carbon–carbon supercapacitors based on organic, aqueous and ionic liquid electrolytes. *J. Power Sources* **2010**, *195*, 5814–5819. [[CrossRef](#)]
24. Béguin, F.; Presser, V.; Balducci, A.; Frackowiak, E. Carbons and Electrolytes for Advanced Supercapacitors. *Adv. Mater.* **2014**, *26*, 2219–2251. [[CrossRef](#)] [[PubMed](#)]
25. Tsai, W.-Y.; Lin, R.; Murali, S.; Li Zhang, L.; McDonough, J.K.; Ruoff, R.S.; Taberna, P.-L.; Gogotsi, Y.; Simon, P. Outstanding performance of activated graphene based supercapacitors in ionic liquid electrolyte from –50 to 80 °C. *Nano Energy* **2013**, *2*, 403–411. [[CrossRef](#)]
26. Van Aken, K.L.; Beidaghi, M.; Gogotsi, Y. Formulation of Ionic-Liquid Electrolyte To Expand the Voltage Window of Supercapacitors. *Angew. Chem. Int. Ed.* **2015**, *54*, 4806–4809. [[CrossRef](#)]
27. Biso, M.; Mastragostino, M.; Montanino, M.; Passerini, S.; Soavi, F. Electropolymerization of poly(3-methylthiophene) in pyrrolidinium-based ionic liquids for hybrid supercapacitors. *Electrochim. Acta* **2008**, *53*, 7967–7971. [[CrossRef](#)]

28. Mousavi, M.P.S.; Wilson, B.E.; Kashefolgheta, S.; Anderson, E.L.; He, S.; Bühlmann, P.; Stein, A. Ionic Liquids as Electrolytes for Electrochemical Double-Layer Capacitors: Structures that Optimize Specific Energy. *ACS Appl. Mater. Interfaces* **2016**, *8*, 3396–3406. [[CrossRef](#)]
29. Wolff, C.; Jeong, S.; Paillard, E.; Balducci, A.; Passerini, S. High power, solvent-free electrochemical double layer capacitors based on pyrrolidinium dicyanamide ionic liquids. *J. Power Sources* **2015**, *293*, 65–70. [[CrossRef](#)]
30. Ue, M. Electrochemical Properties of Organic Liquid Electrolytes Based on Quaternary Onium Salts for Electrical Double-Layer Capacitors. *J. Electrochem. Soc.* **1994**, *141*, 2989. [[CrossRef](#)]
31. Brandt, A.; Isken, P.; Lex-Balducci, A.; Balducci, A. Adiponitrile-based electrochemical double layer capacitor. *J. Power Sources* **2012**, *204*, 213–219. [[CrossRef](#)]
32. Brandt, A.; Balducci, A. The Influence of Pore Structure and Surface Groups on the Performance of High Voltage Electrochemical Double Layer Capacitors Containing Adiponitrile-Based Electrolyte. *J. Electrochem. Soc.* **2012**, *159*, A2053–A2059. [[CrossRef](#)]
33. Chiba, K.; Ueda, T.; Yamaguchi, Y.; Oki, Y.; Shimodate, F.; Naoi, K. Electrolyte Systems for High Withstand Voltage and Durability I. Linear Sulfones for Electric Double-Layer Capacitors. *J. Electrochem. Soc.* **2011**, *158*, A872. [[CrossRef](#)]
34. Laheäär, A.; Jänes, A.; Lust, E. Electrochemical Behavior of Carbide Derived Carbons in LiPF₆ and LiCF₃SO₃ Nonaqueous Electrolytes. *ECS Trans.* **2019**, *28*, 65–75. [[CrossRef](#)]
35. Jänes, A.; Eskusson, J.; Thomberg, T.; Romann, T.; Lust, E. Ionic liquid-1,2-dimethoxyethane mixture as electrolyte for high power density supercapacitors. *J. Energy Chem.* **2016**, *25*, 609–614. [[CrossRef](#)]
36. Ruther, R.E.; Sun, C.-N.; Holliday, A.; Cheng, S.; Delnick, F.M.; Zawodzinski, T.A.; Nanda, J. Stable Electrolyte for High Voltage Electrochemical Double-Layer Capacitors. *J. Electrochem. Soc.* **2016**, *164*, A277–A283. [[CrossRef](#)]
37. Väli, R.; Laheäär, A.; Jänes, A.; Lust, E. Characteristics of non-aqueous quaternary solvent mixture and Na-salts based supercapacitor electrolytes in a wide temperature range. *Electrochim. Acta* **2014**, *121*, 294–300. [[CrossRef](#)]
38. Laheäär, A.; Jänes, A.; Lust, E. NaClO₄ and NaPF₆ as potential non-aqueous electrolyte salts for electrical double layer capacitor application. *Electrochim. Acta* **2012**, *82*, 309–313. [[CrossRef](#)]
39. Mei, X.; Yue, Z.; Tufts, J.; Dunya, H.; Mandal, B.K. Synthesis of new fluorine-containing room temperature ionic liquids and their physical and electrochemical properties. *J. Fluor. Chem.* **2018**, *212*, 26–37. [[CrossRef](#)]
40. Lu, Y.; Zhang, S.; Yin, J.; Bai, C.; Zhang, J.; Li, Y.; Yang, Y.; Ge, Z.; Zhang, M.; Wei, L.; et al. Mesoporous activated carbon materials with ultrahigh mesopore volume and effective specific surface area for high performance supercapacitors. *Carbon* **2017**, *124*, 64–71. [[CrossRef](#)]
41. Zhang, L.; Zhang, F.; Yang, X.; Leng, K.; Huang, Y.; Chen, Y. High-Performance Supercapacitor Electrode Materials Prepared from Various Pollens. *Small* **2013**, *9*, 1342–1347. [[CrossRef](#)] [[PubMed](#)]
42. Wang, X.; Li, Y.; Lou, F.; Melandsø Buan, M.E.; Sheridan, E.; Chen, D. Enhancing capacitance of supercapacitor with both organic electrolyte and ionic liquid electrolyte on a biomass-derived carbon. *RSC Adv.* **2017**, *7*, 23859–23865. [[CrossRef](#)]
43. Simon, P.; Brousse, T.; Favier, F. *Supercapacitors Based on Carbon or Pseudocapacitive Materials*; John Wiley & Sons: Hoboken, NJ, USA, 2017.
44. Wang, J.; Kaskel, S. KOH activation of carbon-based materials for energy storage. *J. Mater. Chem.* **2012**, *22*, 23710–23725. [[CrossRef](#)]
45. Largeot, C.; Portet, C.; Chmiola, J.; Taberna, P.-L.; Gogotsi, Y.; Simon, P. Relation between the Ion Size and Pore Size for an Electric Double-Layer Capacitor. *J. Am. Chem. Soc.* **2008**, *130*, 2730–2731. [[CrossRef](#)]
46. Kameda, Y.; Umebayashi, Y.; Takeuchi, M.; Wahab, M.A.; Fukuda, S.; Ishiguro, S.-i.; Sasaki, M.; Amo, Y.; Usuki, T. Solvation Structure of Li⁺ in Concentrated LiPF₆–Propylene Carbonate Solutions. *J. Phys. Chem. B* **2007**, *111*, 6104–6109. [[CrossRef](#)]
47. Zheng, M.; Hu, Q.; Zhang, S.; Tang, H.; Li, L.; Pang, H. Macroporous Activated Carbon Derived from Rapeseed Shell for Lithium–Sulfur Batteries. *Appl. Sci.* **2017**, *7*, 1036. [[CrossRef](#)]
48. Marzantowicz, M.; Dygas, J.R.; Krok, F.; Łasińska, A.; Florjańczyk, Z.; Zygadło-Monikowska, E.; Affek, A. Crystallization and melting of PEO:LiTFSI polymer electrolytes investigated simultaneously by impedance spectroscopy and polarizing microscopy. *Electrochim. Acta* **2005**, *50*, 3969–3977. [[CrossRef](#)]

49. Laheäär, A.; Kurig, H.; Jänes, A.; Lust, E. LiPF₆ based ethylene carbonate–dimethyl carbonate electrolyte for high power density electrical double layer capacitor. *Electrochim. Acta* **2009**, *54*, 4587–4594. [[CrossRef](#)]
50. Borodin, O.; Behl, W.; Jow, T.R. Oxidative Stability and Initial Decomposition Reactions of Carbonate, Sulfone, and Alkyl Phosphate-Based Electrolytes. *J. Phys. Chem. C* **2013**, *117*, 8661–8682. [[CrossRef](#)]
51. Mei, B.-A.; Munteshari, O.; Lau, J.; Dunn, B.; Pilon, L. Physical Interpretations of Nyquist Plots for EDLC Electrodes and Devices. *J. Phys. Chem. C* **2018**, *122*, 194–206. [[CrossRef](#)]
52. Wu, J.; Liu, W.-W.; Wu, Y.-X.; Wei, T.-C.; Geng, D.; Mei, J.; Liu, H.; Lau, W.-M.; Liu, L.-M. Three-dimensional hierarchical interwoven nitrogen-doped carbon nanotubes/Co_xNi_{1-x}-layered double hydroxides ultrathin nanosheets for high-performance supercapacitors. *Electrochim. Acta* **2016**, *203*, 21–29. [[CrossRef](#)]
53. Kulandaivalu, S.; Suhaimi, N.; Sulaiman, Y. Unveiling high specific energy supercapacitor from layer-by-layer assembled polypyrrole/graphene oxide|polypyrrole/manganese oxide electrode material. *Sci. Rep.* **2019**, *9*, 4884. [[CrossRef](#)] [[PubMed](#)]
54. Wang, Y.; Zhang, Y.; Pei, L.; Ying, D.; Xu, X.; Zhao, L.; Jia, J.; Cao, X. Converting Ni-loaded biochars into supercapacitors: Implication on the reuse of exhausted carbonaceous sorbents. *Sci. Rep.* **2017**, *7*, 41523. [[CrossRef](#)] [[PubMed](#)]
55. Sedlakova, V.; Sikula, J.; Majzner, J.; Sedlak, P.; Kupařowitz, T.; Buegler, B.; Vasina, P. Supercapacitor equivalent electrical circuit model based on charges redistribution by diffusion. *J. Power Sources* **2015**, *286*, 58–65. [[CrossRef](#)]
56. Sedlakova, V.; Sikula, J.; Valsa, J.; Majzner, J.; Dvorak, P. Supercapacitor charge and self-discharge analysis. In Proceedings of the Passive Space Component Days, ESA/ESTEC, Noordwijk, The Netherlands, 24–26 September 2013.
57. Zubieta, L.; Bonert, R. Characterization of double-layer capacitors for power electronics applications. *IEEE Trans. Ind. Appl.* **2000**, *36*, 199–205. [[CrossRef](#)]
58. Graydon, J.W.; Panjehshahi, M.; Kirk, D.W. Charge redistribution and ionic mobility in the micropores of supercapacitors. *J. Power Sources* **2014**, *245*, 822–829. [[CrossRef](#)]
59. Faranda, R. A new parameters identification procedure for simplified double layer capacitor two-branch model. *Electr. Power Syst. Res.* **2010**, *80*, 363–371. [[CrossRef](#)]
60. Sedlakova, V.; Majzner, J.; Josef, S.; Sedlak, P.; Kupařowitz, T.; Buegler, B.; Vasina, P. Supercapacitor Degradation Assessment by Power Cycling and Calendar Life Tests. *Metrol. Meas. Syst.* **2016**, *23*, 345–358. [[CrossRef](#)]
61. Kreczanik, P.; Venet, P.; Hijazi, A.; Clerc, G. Study of Supercapacitor Aging and Lifetime Estimation According to Voltage, Temperature, and RMS Current. *IEEE Trans. Ind. Electron.* **2014**, *61*, 4895–4902. [[CrossRef](#)]
62. Murray, D.B.; Hayes, J.G. Cycle Testing of Supercapacitors for Long-Life Robust Applications. *IEEE Trans. Power Electron.* **2015**, *30*, 2505–2516. [[CrossRef](#)]
63. Rasines, G.; Lavela, P.; Macías, C.; Zafra, M.C.; Tirado, J.L.; Parra, J.B.; Ania, C.O. N-doped monolithic carbon aerogel electrodes with optimized features for the electroadsorption of ions. *Carbon* **2015**, *83*, 262–274. [[CrossRef](#)]
64. Rybarczyk, M.K.; Lieder, M.; Jablonska, M. N-doped mesoporous carbon nanosheets obtained by pyrolysis of a chitosan–melamine mixture for the oxygen reduction reaction in alkaline media. *RSC Adv.* **2015**, *5*, 44969–44977. [[CrossRef](#)]
65. Deng, Y.; Xie, Y.; Zou, K.; Ji, X. Review on recent advances in nitrogen-doped carbons: Preparations and applications in supercapacitors. *J. Mater. Chem. A* **2016**, *4*, 1144–1173. [[CrossRef](#)]
66. Demir, M.; Saraswat, S.K.; Gupta, R.B. Hierarchical nitrogen-doped porous carbon derived from lecithin for high-performance supercapacitors. *RSC Adv.* **2017**, *7*, 42430–42442. [[CrossRef](#)]
67. Kim, K.-S.; Park, S.-J. Synthesis and high electrochemical capacitance of N-doped microporous carbon/carbon nanotubes for supercapacitor. *J. Electroanal. Chem.* **2012**, *673*, 58–64. [[CrossRef](#)]

